Applied Physics Letters ARTICLE pubs.aip.org/aip/apl

Acoustic real second-order nodal-loop semimetal and non-Hermitian modulation

Cite as: Appl. Phys. Lett. **123**, 242201 (2023); doi: 10.1063/5.0173791
Submitted: 25 August 2023 · Accepted: 28 November 2023 ·
Published Online: 13 December 2023

View Online Export Citation CrossMark

Zichong Yue,[1] Zhiwang Zhang,[1,a)] Ying Cheng,[1,2,a)] Xiaojun Liu,[1,2,a)] and Johan Christensen[3,a)]

AFFILIATIONS

[1]Department of Physics, MOE Key Laboratory of Modern Acoustics, Collaborative Innovation Center of Advanced Microstructures, Nanjing University, Nanjing 210093, China
[2]State Key Laboratory of Acoustics, Institute of Acoustics, Chinese Academy of Sciences, Beijing 100190, China
[3]IMDEA Materials Institute, Calle Eric Kandel, 2, 28906 Getafe, Madrid, Spain

Note: This paper is part of the APL Special Collection on Non-Hermitian Photonics.
[a)]**Authors to whom correspondence should be addressed:** zhangzhiwang@nju.edu.cn; chengying@nju.edu.cn; liuxiaojun@nju.edu.cn; and johan.christensen@imdea.org

ABSTRACT

The unique features of spinless time-reversal symmetry and tunable $\mathbb{Z}_2$ gauge fields in artificial systems facilitate the emergence of topological properties in the landscape, such as the recently explored Möbius-twisted phase and real second-order nodal-loop semimetals. However, these properties have predominantly been proposed only in theoretical frameworks. In this study, we present a cunningly designed blueprint for realizing an acoustic real second-order nodal-loop semimetal through the incorporation of projective translation symmetry into a three-dimensional stacked acoustic graphitic lattice. Additionally, we introduce non-Hermitian modulation to the topologically protected propagation of degenerate drumhead surface and hinge states, which depend on the specific on-site gain and loss textures. It should be emphasized that this demonstration can be extended to other classical wave systems, thereby potentially opening up opportunities for the design of functional topological devices.

Topological systems in condensed matter physics have gained significant attention in recent decades due to their rich phenomenology.[1–7] The use of arbitrary designed structures and precise measuring technology makes artificial systems, such as photonics,[8–10] acoustics[11–21] and electric circuits,[22,23] ideal platforms for studying topological phases of matter. Unlike electrons, excitations in artificial systems can have spinless or integer spins under T-reversal symmetry and possess intrinsic $\mathbb{Z}_2$ gauge fields. Thus, there are still numerous unique and intriguing topological phenomena to be explored in classical systems.

Most recently, it has been discovered that spatial symmetries can be represented projectively under a gauge field, leading to the realization of intriguing topological phases.[24–34] For instance, theoretical proposals include Kramers degenerate bands and Majorana boundary states in spinless systems, as well as real Stiefel–Whitney topological phases in spinful systems. The switching between spinless and spinful topological phases and the three-dimensional real second-order nodal-loop semimetal (SNOOPI) can be achieved under the projective space-time inversion symmetry.[25,27–29] Notably, only a subset of the aforementioned theories have been confirmed in artificial systems, such as Möbius-twisted topological phases and the spinless/spinful switching process.[30–32] Most recently, a second-order nodal-loop topological semimetal was experimentally reported based on a three-dimensional rectangular sonic crystal.[34]

In this study, we present a blueprint design for an acoustic model that achieves the realization of a real SNOOPI system. Our approach involves utilizing a 3D graphite lattice with coupled cavities, arranged in a stacked configuration, which supports the inherent fourfold Dirac point. By introducing negative couplings, the interlayer flux of π is obtained and the real Dirac points come in pairs, obeying the Nielsen–Ninomiya No-go theorem.[25] After applying alternating dimerization, i.e., modulating the interlayer couplings between different sites alternatively, each Dirac point is split into a real nodal loop. In comparison with the previously reported acoustic topological semimetals[35–42] and higher-order topological semimetals,[43–46] our acoustic real SNOOPI system demonstrates a distinct characteristic of possessing a double degeneracy of drumhead surface and hinge states. Finally, we further add on-site non-Hermitian gain and loss,[16,47–50] resulting in preserved topology, yet in the presence of either amplifying or attenuating states, which enriches the categories of topological semimetals incorporating artificial gauge field.

We begin with a tight-binding model (TBM) of the SNOOPI as shown in Fig. 1(a), which is formed by 3D stacking the coupled graphite layers with sites A and B under projective translation symmetries. Note that the couplings between the nearest sites in each single layer are denoted by blue lines with a strength of t. Red dashed lines indicate the negative interlayer couplings of sites A, while positive interlayer couplings are labeled by green solid lines connecting sites B of different layers. The alternating strength (J_1 and J_2) of the negative/positive coupling is further considered, as depicted in Fig. 1(a). The corresponding Hamiltonian of this model can be written as

$$\mathcal{H}(\boldsymbol{k}) = \sum_{i=1}^{4} f_i(\boldsymbol{k})\Gamma^i + g_1(k_z)i\Gamma^4\Gamma^5 + g_2(k_z)i\Gamma^3\Gamma^5, \qquad (1)$$

with $f_1(\boldsymbol{k}) + if_2(\boldsymbol{k}) = t\sum_{i=1}^{3} e^{-i\boldsymbol{k}\boldsymbol{a}_i}$, where $\boldsymbol{a}_i$ represents the three bond vectors for each hexagonal layer. In Eq. (1), $f_3(\boldsymbol{k}) = (J_1 + J_2)(1+\cos(k_y))/2$, $f_4(\boldsymbol{k}) = (J_1+J_2)\sin(k_y)/2$, $g_1(k_z) = (J_1-J_2)(1-\cos(k_y))/2$, $g_2(k_z) = (J_1-J_2)\sin(k_y)/2$, $\Gamma^1 = \tau_0\otimes\sigma_1$, $\Gamma^2 = \tau_0\otimes\sigma_2$, $\Gamma^3 = \tau_1\otimes\sigma_3$, $\Gamma^4 = \tau_2\otimes\sigma_3$, and $\Gamma^5 = \tau_3\otimes\sigma_3$, where τ and σ are two sets of the Pauli matrices that parameterize a unit cell. In the right panel of Fig. 1(a), it can be observed that every interlayer rectangular plaquette encloses a π flux under the $\mathbb{Z}_2$ gauge fields.[29] There exist mirror symmetry M_y through the zx-plane and the primitive translation L_z along the z direction, which apply the anticommutation relation of $\{M_z, L_z\} = 0$. It has been proven that the corner K in 3D BZ is invariant under the D_3 group. The projective algebraic relations correspond to the group $D_3 \times \mathbb{Z}_2$ given by

$$\{L_z^K, M\} = \{L_z^K, R_\pi T\} = 0, \quad (L_z^K)^2 = -1,$$

where R_ϕ is the ϕ rotation along the z axis (see the supplementary material).[28,34] By setting $t = J_1 = J_2 = 1$, a fourfold real Dirac point emerges at the corners of the folded Brillouin zone (BZ), which can be found in the calculated band structure depicted in Fig. 1(b). With the extended $k\cdot p$ method, highly degenerate Fermi points corresponding to higher-dimensional irreducible representations (IRREPs) of the modified little co-group can be generated. For our graphite lattice model, the little co-group G_K has 4D IRREPs (see the supplementary material for the detail analysis). Thus, there exist fourfold Dirac points. In addition, the fourfold real Dirac points are protected by PT symmetry due to $(PT)^2 = 1$, which have been proved in previous literature.[28,34] To identify the positions of Dirac points in the reciprocal space, a complete band structure at the plane of $k_z = \pi/a_z$ is plotted in Fig. 1(c), where a_z represents the lattice constant along the z direction. The color contour of the bands illustrates the energy variation relative to the zero-energy Fermi level, with the red labels signifying the minimum value representing the band degeneracy. From the projection, we can clearly observe six Dirac points at the BZ corners. In this case, the stacking of two Weyl points with opposite chiralities in the unfolded BZ explains the presence of Dirac points. The supplementary material provides an explanation of the associated band folding mechanism. Next, the alternating dimerization with $J_1 \neq J_2$ is taken into considerations, and the calculated band structure of the TBM is shown in Fig. 1(d). We find that the Dirac degeneracy is lifted, but a doubly degenerate nodal loop appears between points A and H of the BZ. Seen in the complete band structure in Fig. 1(e), a real nodal loop normal to the k_z direction around BZ corners is formed.

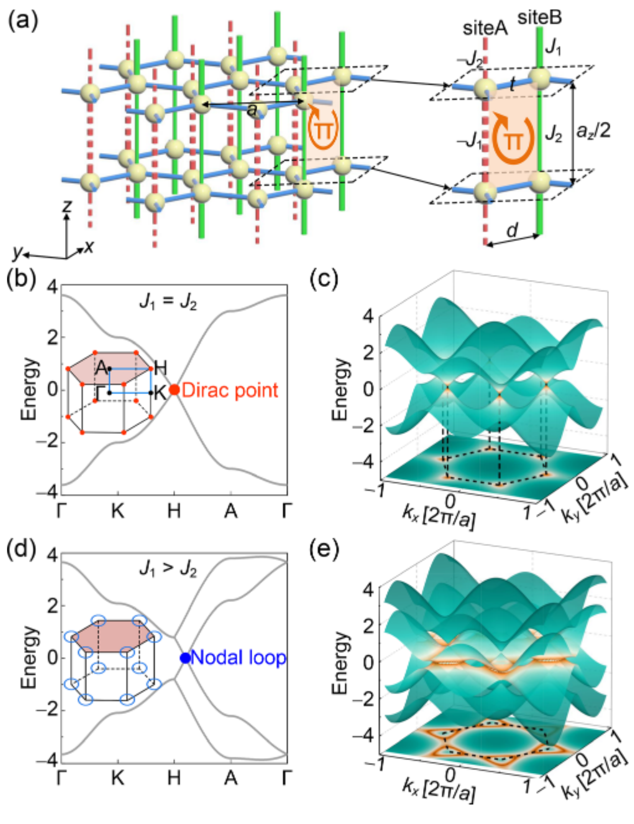

FIG. 1. Theoretical tight-binding model of the SNOOPI. (a) Illustration of the model built by a 3D stacked graphite lattice. The right panel shows the unit cell. (b) Theoretical and (c) complete band structures for the undimerized lattice with $J_1 = J_2 = t = 1$ at the plane $k_z = \pi/a_z$. Inset: locations of Dirac points in the reciprocal space. (d) and (e) The same as (b) and (c), but for the dimerized lattice with $t = 1$, $J_1 = 1.44$, and $J_2 = 0.64$. Inset: locations of nodal loops.

We extend the TBM to account for positive/negative couplings and dimerization in the real acoustic SNOOPI shown in Fig. 2(a). Usually, a pair of identical air cavities coupled with narrow tubes are utilized to achieve acoustic positive/negative couplings through varying the positions of the tubes in 2D systems.[51] However, due to the much more complex structures in 3D sonic crystal, the positions of the coupling tubes need to be altered on demand, which may significantly affect the eigenfrequencies of the acoustic resonators in such systems and lead to some inevitable problems during the designing process. To overcome this obstacle, we propose a unit cell of 3D stacked sonic lattice as shown in the inset of Fig. 2(a), where each site (colored by yellow) is composed of two cavities with a radius of $r = 16.15$ mm connected by a cylindrical tube with a radius of 5.65 mm. The distance between these two cavities is set to 56 mm. Compared with the previously reported protocols, our structure supports the lower resonant frequency and enables arbitrary modulation of the direction of the coupling tubes while keeping the acoustic resonant frequencies stable (see the supplementary material). The couplings between the nearest sites in each single layer are mimicked by the V-shaped blue tubes

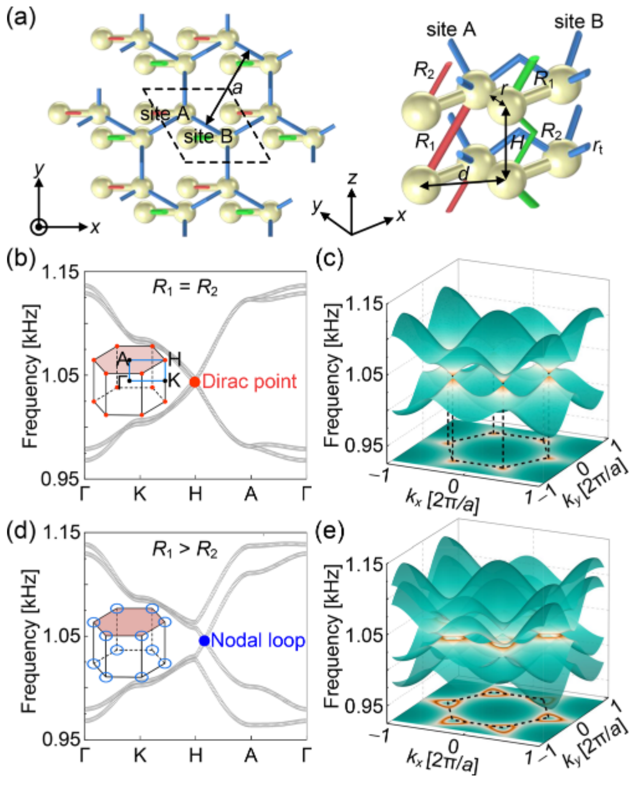

FIG. 2. Acoustic structure of the cunningly designed SNOOPI. (a) Structural schematic of the designed acoustic SNOOPI made of coupled cavities. The right panel shows the unit cell. (b) Theoretical and (c) complete band structure for the sonic lattice with $R_1 = R_2 = r_t = 3$ mm at the plane of $k_z = 0.5\pi/H$. The color represents the absolute frequency difference between the band and the Dirac point. (d) and (e) The same as (b) and (c), but introduces the alternating dimerization with $R_1 > R_2$.

with radius $r_t = 3$ mm and a total length of 89.64 mm. The lattice constant of the graphite layer is $a = \sqrt{3}d$ with $d = 70$ mm. The interlayer positive/negative couplings can be modulated by adjusting the radii of the alternating green/red tubes to R_1 and R_2. The interval between each layer is $H = 70$ mm, resulting in a period of $a_z = 2H$ along the z direction. The simulations presented in this work are calculated using the commercial finite-element-method software COMSOL Multiphysics. The standard parameters for air are the mass density $\rho_0 = 1.21$ kg/m^3 and sound speed $c_0 = 343$ m/s. With the interlayer couplings fixed at $R_1 = R_2 = r_t = 3$ mm, the dispersion relation of the sonic crystal shown in Figs. 2(b) and 2(c) contains a fourfold degenerate Dirac point at each BZ corner around the frequency of 1044 Hz, which aligns well with the TBM prediction in Figs. 1(b) and 1(c). Note that the simulated acoustic bands are not strictly twofold degenerate, which can be ascribed to the presence of the inevitable long-range couplings and the interactions among different acoustic modes in such cavity-tube-coupled sonic crystals. In Figs. 2(d) and 2(e), the Dirac points are split into nodal loops normal to the k_z direction when the radii of the coupling tubes are changed to $R_1 = 3.6$ and $R_2 = 2.4$ mm. We emphasize that the discussed real nodal loop possesses both a first and second Stiefel–Whitney topological charges,[27,28] giving rise to degenerate drumhead surface and hinge states as will be discussed in the following. The details for calculating the topological invariant can be found in the supplementary material.

To investigate the drumhead surface states in the acoustic SNOOPI, we calculate the band diagrams of a semi-infinite sonic crystal as shown in Fig. 3. First, the structure consists of 14 units along the direction with an angle of 30° to the y axis, while it extends infinitely along the other two directions. The dispersion relations at the plane of $k_z = \pi/a_z = 0.5\pi/H$ are shown in Fig. 3(a), with the geometrical parameters identical to those in Figs. 2(d) and 2(e). Notably, degenerate drumhead surface states are identified around the frequencies of 1030 and 1063 Hz, indicated by blue dots in Fig. 3(a). Additional boundary cells are included at the termination to emulate the open boundary condition in the TBM,[17,52–54] which ensures the degeneracy of boundary states (see the supplementary material for the theoretical results from TBM). Simulated acoustic pressure field distributions of the surface eigenstates are presented in Fig. 3(b), which confine sound energy tightly at the external surfaces parallel to the xz-plane. Remarkably, the eigenstates (i) and (ii) exhibit anti-symmetric patterns, while the eigenstates (iii) and (iv) display symmetric ones. To further explore the behavior of the structure, Fig. 3(c) illustrates the dispersion relations when the structure is finite along the z direction (with 15 layers) but infinite along the other two directions. The clearly observed degenerate bands of the drumhead surface states explicate

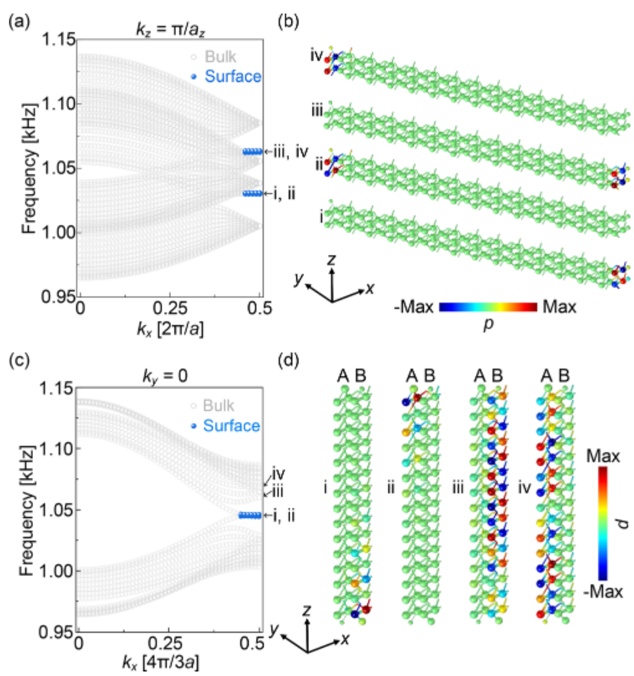

FIG. 3. (a) Dispersion relations of the acoustic semi-infinite structure with periodic boundary conditions along the x and z directions. Wave number k_z is pinned at $k_z = \pi/a_z$. Bulk and drumhead surfaces states are labeled as gray circles and blue dots, respectively. (b) Simulated acoustic pressure field distribution of the eigenstates for the drumhead surfaces states marked in (a). (c) and (d) The same as (a) and (b), but for the acoustic structure with the finite size along the z direction but periodic boundary conditions along other two directions instead. Wave number k_y is pinned at $k_y = 0$. Acoustic profiles of the bulk states are also illustrated in (d).

the characteristic of the nodal loop. For comparison, acoustic profiles of both bulk and surface states are presented in Fig. 3(d), where sound spreads into the bulk for eigenstates (iii) and (iv), but propagates along the external surfaces parallel to the xy-plane for eigenstates (i) and (ii).

Beyond demonstrating the 2D drumhead surface states, we continue to study 1D hinge states propagating along the hinge of the acoustic SNOOPI. A supercell, depicted in Fig. 4(b), is designed based on the same geometrical parameters as Figs. 2(d) and 2(e), with infinite extension along the x direction, eight units along a direction at an angle of 30° to the y axis, and 15 layers along the z direction to ensure inversion symmetry. We observe a pair of degenerate hinge states labeled by red dots in Fig. 4(a) around the central frequency of $f = 1044$ Hz while scanning along k_x. Note that the hinge states only exist in the right bandgap, which is protected by the nontrivial topological invariant in this region as discussed in the supplementary material. The acoustic profiles in Fig. 4(b) demonstrate that the states exist only along the diagonal hinges, unlike their off diagonal counterparts. This can be attributed to the characteristics of the drumhead surface states shown in Fig. 3, where sound waves are confined solely to site-A cavities along the top xy-plane and only to site-B cavities along the bottom xy-plane. We demonstrate that the positions of the hinge states can be reversed to become off diagonal by alternating the dimerization factors J_1 and J_2. Additionally, we provide a numerical discussion of the topological hinge states in the frequency domain. For this purpose, a $6 \times 8 \times 15$ 3D acoustic SNOOPI is designed, as shown in Fig. 4(c). A point source, marked by a red star, is placed at the desired position along different hinges. By appropriately setting the excitation frequency, hinges I and III can be excited, as depicted in Fig. 4(c). However, as shown in Fig. 4(d), hinges II and IV are not excited, which is consistent with the previous discussion.

Finally, we extend the investigation of SNOOPI by introducing non-Hermiticity in terms of on-site gain and loss, as shown in Fig. 5(a). The Hamiltonian can be written as

$$\mathcal{H}(\boldsymbol{k}) = \sum_{i=1}^{4} f_i(\boldsymbol{k})\Gamma^i + g_1(k_z)i\Gamma^4\Gamma^5 + g_2(k_z)i\Gamma^3\Gamma^5 - gi\Gamma^6, \quad (2)$$

where $\Gamma^6 = \tau_0 \otimes \sigma_3$, and g represents the amount of gain/loss. We employ the active acoustic metamaterials with an effective complex sound velocity to serve as the acoustic gain and loss. To balance gain and loss, each unit consists of two gain sites and two loss sites. Specifically, the effective velocity in the site-A cavities is defined as $c_{\text{loss}} = (1 + i\beta)c_0$ for the loss component, and that in site-B cavities is $c_{\text{gain}} = (1 - i\beta)c_0$ for the gain component. Here, β represents the non-Hermitian factor. The mass density is kept as ρ_0. Fixing the non-Hermitian factor to $\beta = 0.01$, we examine the drumhead surface states in the xy-plane by calculating the dispersion relations of the ribbon-shaped structure as was done in Fig. 3(a). The real band diagrams in Fig. 5(b) show identical results with the Hermitian case, and the degenerate drumhead surface states can still be obtained. When zooming into the complex bands of the anti-symmetric surfaces states (i) and (ii) as displayed in Fig. 5(c), the eigenfrequencies are found to be complex conjugate. This indicates that the states (i) confined to the right surface have negative imaginary frequencies, signifying amplifying states. On the other hand, the states (ii) on the left surface have positive imaginary frequencies, suggesting attenuation of the acoustic states. Figure 5(d) shows the real band diagram for the structure, which is finite along

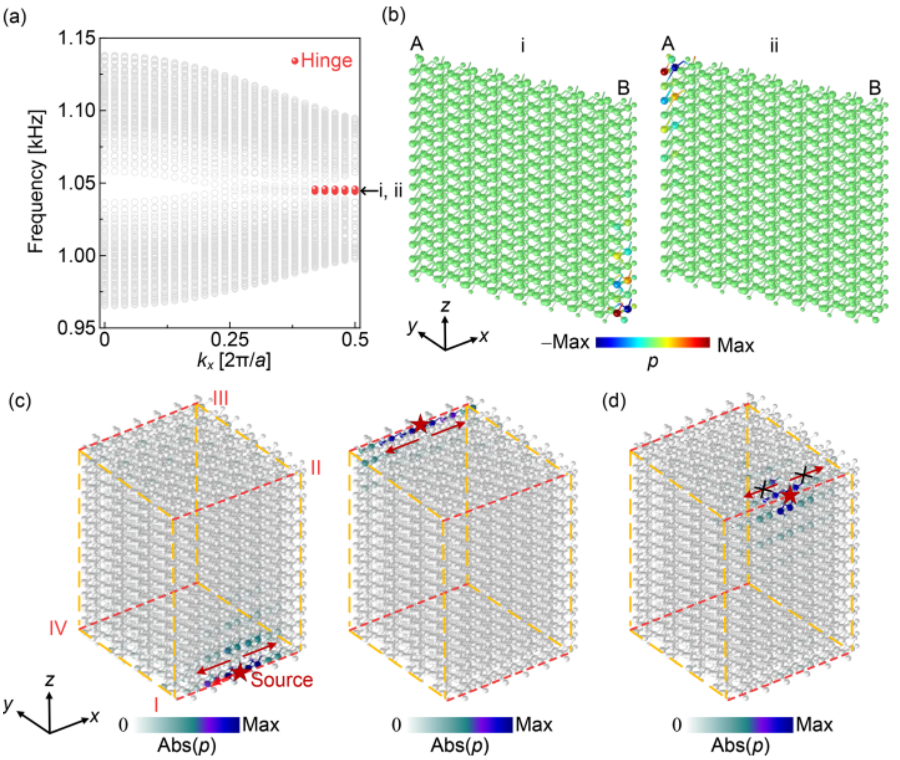

FIG. 4. (a) Simulated dispersion based on a super cell, which is infinite along the x direction but finite along other directions. (b) Acoustic profiles of the hinge eigenstates along the x direction as marked in (a). (c) and (d) Simulated distributions of the pressure fields when placing a point source at (c) the hinges I and III and (d) the hinge II.

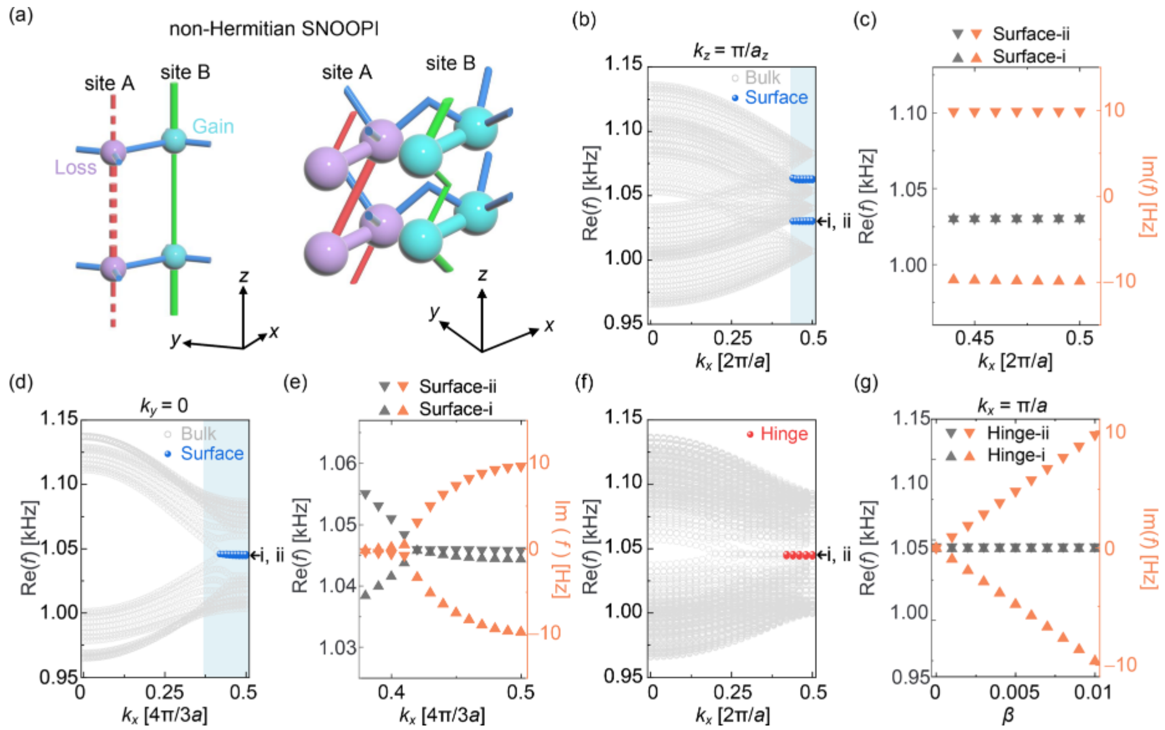

FIG. 5. (a) TBM (left panel) and acoustic structure (right panel) of the SNOOPI in the presence of non-Hermiticity. (b) Real dispersion relations of the acoustic structure with the finite size along the direction with an angle of 30° to y axis. (c) The complex dispersion relations of surface states in the shaded area as shown in (b). (d) and (e) The same as (b) and (c), but for the structure with the finite size along the z direction but periodic boundary conditions along other two directions. (f) Simulated dispersion for super cell infinite along the x direction but finite along both y and z directions after introducing gain/loss components. (g) The complex eigenfrequencies of the hinge states are calculated with varying β.

the z direction as discussed in Fig. 3(c). Two of the bulk bands intersect at the nodal loops, become degenerate, and act as surface states afterward. As evident from the zoom-in view of the complex dispersion relation [Fig. 5(e)], the bulk bands are purely real before approaching the nodal loop, beyond which they transform into complex conjugate surface states. The non-Hermitian modulation of the hinge states is also analyzed in Fig. 5(f). In Fig. 5(g), the complex hinge states (i) and (ii) for $k_x = \pi/a$ are computed as a function of β. Their imaginary counterparts clearly display a thresholdless phase transition as the complex conjugate states grow linearly with β.

In conclusion, we have designed a realistic SNOOPI utilizing acoustic waves. By introducing positive and negative couplings, we obtain degenerate bands and fourfold Dirac points. The Dirac points are lifted by the alternating dimerization, resulting in doubly degenerate nodal loops. The combined space-time inversion symmetry of the acoustic SNOOPI enables the presence of both ordinary drumhead surface states and a pair of states confined along the diagonal hinges. In addition, we study the influence of non-Hermiticity by introducing acoustic gain and loss. We found that the added non-Hermitian component is able to render the surface hinge states either amplifying or attenuating. Our study demonstrates the potential to expose more intriguing topological phases of matter, by exploring the projective symmetry and non-Hermiticity in accessible acoustic settings.

See the supplementary material for explanation of the irreducible representation and symmetry, the band folding mechanism, advantages of our proposed structures, topological invariants of the stacked graphite lattice model, calculated dispersion relations of the ribbon-shaped structure from TBM, and the location of the hinge states.

We acknowledge Y. X. Zhao for fruitful discussions. This work was supported by the National Key R&D Program of China (Nos. 2022YFA1404500 and 2022YFA1404400), NSFC (Nos. 12074183, 11834008, 12104226, 12227809, and 12225408), and the Fundamental Research Funds for the Central Universities (Nos. 020414380181, and 020414380211). Z.Z. acknowledges support from the Funds for Zijin Scholars of Nanjing University. J.C. acknowledges support from the Spanish Ministry of Science and Innovation through a Consolidación Investigadora grant (No. CNS2022-135706).

AUTHOR DECLARATIONS

Conflict of Interest

The authors have no conflicts to disclose.

Author Contributions

Zichong Yue: Data curation (equal); Investigation (equal); Methodology (equal); Visualization (equal); Writing – original draft (lead). **Zhiwang Zhang:** Conceptualization (lead); Funding acquisition (equal); Supervision (equal); Validation (equal); Writing – review & editing (equal). **Ying Cheng:** Funding acquisition (equal); Supervision (equal); Validation (equal); Writing – review & editing (equal). **Xiaojun Liu:** Funding acquisition (equal); Supervision (equal); Validation (equal); Writing – review & editing (equal). **Johan Christensen:** Supervision (equal); Validation (equal); Writing – review & editing (equal).

DATA AVAILABILITY

The data that support the findings of this study are available from the corresponding authors upon reasonable request.

REFERENCES

[1]M. Z. Hasan and C. L. Kane, "Colloquium: Topological insulators," Rev. Mod. Phys. **82**, 3045 (2010).
[2]X.-L. Qi and S.-C. Zhang, "Topological insulators and superconductors," Rev. Mod. Phys. **83**, 1057–1110 (2011).
[3]T. Ozawa, H. M. Price, A. Amo, N. Goldman, M. Hafezi, L. Lu, M. C. Rechtsman, D. Schuster, J. Simon, O. Zilberberg, and I. Carusotto, "Topological photonics," Rev. Mod. Phys. **91**, 015006 (2019).
[4]X. Zhang, F. Zangeneh-Nejad, Z.-G. Chen, M.-H. Lu, and J. Christensen, "A second wave of topological phenomena in photonics and acoustics," Nature **618**, 687–697 (2023).
[5]S. D. Huber, "Topological mechanics," Nat. Phys. **12**, 621–623 (2016).
[6]N. R. Cooper, J. Dalibard, and I. B. Spielman, "Topological bands for ultracold atoms," Rev. Mod. Phys. **91**, 015005 (2019).
[7]B. Xie, H.-X. Wang, X. Zhang, P. Zhan, J.-H. Jiang, M. Lu, and Y. Chen, "Higher-order band topology," Nat. Rev. Phys. **3**, 520–532 (2021).
[8]L. Lu, J. D. Joannopoulos, and M. Soljačić, "Topological photonics," Nat. Photonics **8**, 821–829 (2014).
[9]J.-W. Dong, X.-D. Chen, H. Zhu, Y. Wang, and X. Zhang, "Valley photonic crystals for control of spin and topology," Nat. Mater. **16**, 298–302 (2017).
[10]Y. Yang, Z. Gao, H. Xue, L. Zhang, M. He, Z. Yang, R. Singh, Y. Chong, B. Zhang, and H. Chen, "Realization of a three-dimensional photonic topological insulator," Nature **565**, 622–626 (2019).
[11]Z. Yang, F. Gao, X. Shi, X. Lin, Z. Gao, Y. Chong, and B. Zhang, "Topological acoustics," Phys. Rev. Lett. **114**, 114301 (2015).
[12]J. Lu, C. Qiu, L. Ye, X. Fan, M. Ke, F. Zhang, and Z. Liu, "Observation of topological valley transport of sound in sonic crystals," Nat. Phys. **13**, 369–374 (2017).
[13]Z. Zhang, Q. Wei, Y. Cheng, T. Zhang, D. Wu, and X. Liu, "Topological creation of acoustic pseudospin multipoles in a flow-free symmetry-broken metamaterial lattice," Phys. Rev. Lett. **118**, 084303 (2017).
[14]F. Li, X. Huang, J. Lu, J. Ma, and Z. Liu, "Weyl points and fermi arcs in a chiral phononic crystal," Nat. Phys. **14**, 30–34 (2018).
[15]H. He, C. Qiu, L. Ye, X. Cai, X. Fan, M. Ke, F. Zhang, and Z. Liu, "Topological negative refraction of surface acoustic waves in a weyl phononic crystal," Nature **560**, 61–64 (2018).
[16]Z. Zhang, M. Rosendo López, Y. Cheng, X. Liu, and J. Christensen, "Non-Hermitian sonic second-order topological insulator," Phys. Rev. Lett. **122**, 195501 (2019).
[17]X. Ni, M. Weiner, A. Alu, and A. B. Khanikaev, "Observation of higher-order topological acoustic states protected by generalized chiral symmetry," Nat. Mater. **18**, 113–120 (2019).
[18]P. Gao, D. Torrent, F. Cervera, P. San-Jose, J. Sánchez-Dehesa, and J. Christensen, "Majorana-like zero modes in Kekulé distorted sonic lattices," Phys. Rev. Lett. **123**, 196601 (2019).
[19]B. Hu, Z. Zhang, H. Zhang, L. Zheng, W. Xiong, Z. Yue, X. Wang, J. Xu, Y. Cheng, X. Liu *et al.*, "Non-Hermitian topological whispering gallery," Nature **597**, 655–659 (2021).
[20]L.-Y. Zheng and J. Christensen, "Dirac hierarchy in acoustic topological insulators," Phys. Rev. Lett. **127**, 156401 (2021).
[21]H. Qiu, Q. Zhang, T. Liu, X. Fan, F. Zhang, and C. Qiu, "Minimal non-abelian nodal braiding in ideal metamaterials," Nat. Commun. **14**, 1261 (2023).
[22]S. Imhof, C. Berger, F. Bayer, J. Brehm, L. W. Molenkamp, T. Kiessling, F. Schindler, C. H. Lee, M. Greiter, T. Neupert *et al.*, "Topolectrical-circuit realization of topological corner modes," Nat. Phys. **14**, 925–929 (2018).
[23]R. Yu, Y. Zhao, and A. P. Schnyder, "4D spinless topological insulator in a periodic electric circuit," Natl. Sci. Rev. **7**, 1288–1295 (2020).
[24]Y. X. Zhao and Z. D. Wang, "Novel $\mathbb{Z}_2$ topological metals and semimetals," Phys. Rev. Lett. **116**, 016401 (2016).
[25]Y. X. Zhao and Y. Lu, "PT-symmetric real Dirac fermions and semimetals," Phys. Rev. Lett. **118**, 056401 (2017).
[26]Y. X. Zhao, Y.-X. Huang, and S. A. Yang, "$\mathbb{Z}_2$-projective translational symmetry protected topological phases," Phys. Rev. B **102**, 161117 (2020).
[27]K. Wang, J.-X. Dai, L. Shao, S. A. Yang, and Y. Zhao, "Boundary criticality of PT-invariant topology and second-order nodal-line semimetals," Phys. Rev. Lett. **125**, 126403 (2020).
[28]L. B. Shao, Q. Liu, R. Xiao, S. A. Yang, and Y. X. Zhao, "Gauge-field extended $k \cdot p$ method and novel topological phases," Phys. Rev. Lett. **127**, 076401 (2021).
[29]Y. X. Zhao, C. Chen, X.-L. Sheng, and S. A. Yang, "Switching spinless and spinful topological phases with projective PT symmetry," Phys. Rev. Lett. **126**, 196402 (2021).
[30]H. Xue, Z. Wang, Y.-X. Huang, Z. Cheng, L. Yu, Y. X. Foo, Y. X. Zhao, S. A. Yang, and B. Zhang, "Projectively enriched symmetry and topology in acoustic crystals," Phys. Rev. Lett. **128**, 116802 (2022).
[31]T. Li, J. Du, Q. Zhang, Y. Li, X. Fan, F. Zhang, and C. Qiu, "Acoustic Möbius insulators from projective symmetry," Phys. Rev. Lett. **128**, 116803 (2022).
[32]Y. Meng, S. Lin, B-j Shi, B. Wei, L. Yang, B. Yan, Z. Zhu, X. Xi, Y. Wang, Y. Ge, S-q Yuan, J. Chen, G.-G. Liu, H-x Sun, H. Chen, Y. Yang, and Z. Gao, "Spinful topological phases in acoustic crystals with projective PT symmetry," Phys. Rev. Lett. **130**, 026101 (2023).
[33]T. Li, L. Liu, Q. Zhang, and C. Qiu, "Acoustic realization of projective mirror Chern insulators," Commun. Phys. **6**, 268 (2023).
[34]H. Xue, Z. Y. Chen, Z. Cheng, J. X. Dai, Y. Long, Y. X. Zhao, and B. Zhang, "Stiefel-Whitney topological charges in a three-dimensional acoustic nodal-line crystal," Nat. Commun. **14**, 4563 (2023).
[35]H. Qiu, C. Qiu, R. Yu, M. Xiao, H. He, L. Ye, M. Ke, and Z. Liu, "Straight nodal lines and waterslide surface states observed in acoustic metacrystals," Phys. Rev. B **100**, 041303 (2019).
[36]Y. Yang, J.-P. Xia, H.-X. Sun, Y. Ge, D. Jia, S.-Q. Yuan, S. A. Yang, Y. Chong, and B. Zhang, "Observation of a topological nodal surface and its surface-state arcs in an artificial acoustic crystal," Nat. Commun. **10**, 5185 (2019).
[37]X. Wu, X. Li, R.-Y. Zhang, X. Xiang, J. Tian, Y. Huang, S. Wang, B. Hou, C. T. Chan, and W. Wen, "Deterministic scheme for two-dimensional type-II Dirac points and experimental realization in acoustics," Phys. Rev. Lett. **124**, 075501 (2020).
[38]M. Xiao, L. Ye, C. Qiu, H. He, Z. Liu, and S. Fan, "Experimental demonstration of acoustic semimetal with topologically charged nodal surface," Sci. Adv. **6**, eaav2360 (2020).
[39]H. He, C. Qiu, X. Cai, M. Xiao, M. Ke, F. Zhang, and Z. Liu, "Observation of quadratic Weyl points and double-helicoid arcs," Nat. Commun. **11**, 1820 (2020).
[40]J. Lu, X. Huang, M. Yan, F. Li, W. Deng, and Z. Liu, "Nodal-chain semimetal states and topological focusing in phononic crystals," Phys. Rev. Appl. **13**, 054080 (2020).
[41]B. Jiang, A. Bouhon, Z.-K. Lin, X. Zhou, B. Hou, F. Li, R.-J. Slager, and J.-H. Jiang, "Experimental observation of non-Abelian topological acoustic semimetals and their phase transitions," Nat. Phys. **17**, 1239–1246 (2021).
[42]M. Wang, S. Liu, Q. Ma, R.-Y. Zhang, D. Wang, Q. Guo, B. Yang, M. Ke, Z. Liu, and C. Chan, "Experimental observation of non-Abelian earring nodal links in phononic crystals," Phys. Rev. Lett. **128**, 246601 (2022).
[43]H.-X. Wang, Z.-K. Lin, B. Jiang, G.-Y. Guo, and J.-H. Jiang, "Higher-order Weyl semimetals," Phys. Rev. Lett. **125**, 146401 (2020).
[44]L. Luo, H.-X. Wang, Z.-K. Lin, B. Jiang, Y. Wu, F. Li, and J.-H. Jiang, "Observation of a phononic higher-order Weyl semimetal," Nat. Mater. **20**, 794–799 (2021).
[45]H. Qiu, M. Xiao, F. Zhang, and C. Qiu, "Higher-order Dirac sonic crystals," Phys. Rev. Lett. **127**, 146601 (2021).
[46]Q. Wei, X. Zhang, W. Deng, J. Lu, X. Huang, M. Yan, G. Chen, Z. Liu, and S. Jia, "Higher-order topological semimetal in acoustic crystals," Nat. Mater. **20**, 812–817 (2021).

[47] L. Zhang, Y. Yang, Y. Ge, Y.-J. Guan, Q. Chen, Q. Yan, F. Chen, R. Xi, Y. Li, D. Jia *et al.*, "Acoustic non-Hermitian skin effect from twisted winding topology," Nat. Commun. **12**, 6297 (2021).
[48] X. Zhang, Y. Tian, J.-H. Jiang, M.-H. Lu, and Y.-F. Chen, "Observation of higher-order non-Hermitian skin effect," Nat. Commun. **12**, 5377 (2021).
[49] H. Gao, H. Xue, Z. Gu, T. Liu, J. Zhu, and B. Zhang, "Non-Hermitian route to higher-order topology in an acoustic crystal," Nat. Commun. **12**, 1888 (2021).
[50] B. Hu, Z. Zhang, Z. Yue, D. Liao, Y. Liu, H. Zhang, Y. Cheng, X. Liu, and J. Christensen, "Anti-parity-time symmetry in a Su-Schrieffer-Heeger sonic lattice," Phys. Rev. Lett. **131**, 066601 (2023).
[51] Y. Qi, C. Qiu, M. Xiao, H. He, M. Ke, and Z. Liu, "Acoustic realization of quadrupole topological insulators," Phys. Rev. Lett. **124**, 206601 (2020).
[52] Z. Pu, H. He, L. Luo, Q. Ma, L. Ye, M. Ke, and Z. Liu, "Acoustic higher-order Weyl semimetal with bound hinge states in the continuum," Phys. Rev. Lett. **130**, 116103 (2023).
[53] D. Liao, Z. Yue, Z. Zhang, H.-X. Wang, Y. Cheng, and X. Liu, "Observations of Tamm modes in acoustic topological insulators," Appl. Phys. Lett. **120**, 211701 (2022).
[54] D. Liao, Z. Zhang, Y. Cheng, and X. Liu, "Engineering negative coupling and corner modes in a three-dimensional acoustic topological network," Phys. Rev. B **105**, 184108 (2022).